Journal of Radioanalytical and Nuclear Chemistry (2023) 332:2971–2987
https://doi.org/10.1007/s10967-023-08977-3

Sorption behavior of ^{137}Cs, $^{152+154}$Eu and ^{131}Ba from aqueous solutions using inorganic sorbent loaded on talc

Muhammad S. Mansy[1,2] · Marwa A. Eid[3] · Mohamed M. E. Breky[4] · Mohamed R. Abass[5]

Received: 21 December 2022 / Accepted: 24 May 2023 / Published online: 28 June 2023

Abstract
Iron phosphate@talc (IPT) sorbent was fabricated by precipitation method and utilized for ^{137}Cs, $^{152+154}$Eu, and ^{131}Ba sorption from aqueous media. Different analytical apparatuses such as XRD, FT-IR, SEM, and XRF were used to find the structure, morphology, and functional groups of IPT sorbent. Different parameters like shaking time, pH, temperature, and initial metal concentrations were studied. The obtained data reveal that the sorption of ^{137}Cs, $^{152+154}$Eu, and ^{131}Ba was pH, time-dependence, and kinetics following pseudo-2nd-order kinetics. The Langmuir and Freundlich equations were used as model isotherms. Thermodynamics parameters were calculated to prove that the sorption reaction was spontaneous and endothermic.

Keywords ^{137}Cs · $^{152+154}$Eu · ^{131}Ba · Talc · Inorganic sorbent · Iron phosphate

Introduction

Because of modern science and technology development, nuclear energy is now widely used for civilian purposes in fields including industry, agriculture, medicine, and scientific research. Moreover, the nuclear industry is rapidly expanding and provides a significant amount of solid, liquid, and gaseous radioactive waste, which should be treated properly before being adequately disposed of [1]. These radioactive waste forms are classified into low, intermediate, and high levels, with liquid radioactive waste representing a large segment of the total [2]. Radionuclides in liquid radioactive waste are normally categorized into two categories fission products (such as ^{137}Cs, ^{90}Sr, $^{152+154+155}$Eu, ^{133}Ba, etc.) and activation products (such as ^{63}Ni, ^{60}Co, ^{56}Fe) [3]. The most problematic constituents in radioactive liquid wastes are barium, europium, strontium, and cesium because they are long-lived radionuclides [4, 5]. Due to this, it is extremely important to get eliminate them from liquid waste streams before they are discharged into the environment. However, some beneficial radionuclides are recovered for use in various applications, such as creating a ^{137}Cs/^{137m}Ba radioisotope generator used in industry and medicine for quality control and the production of sealed sources employing $^{152+154}$Eu for use in industry and health [3, 6]. Ion exchange [7, 8], chemical precipitation [9], membrane separation [10, 11], solvent extraction [12], and adsorption [13, 14] are examples of techniques and methodologies that have been developed for the treatment of aqueous radioactive waste. Adsorption is an efficient and cost-effective technique to concentrate and remove contaminants from the aqueous phases. The contaminants are recovered from the aqueous solutions and bound in artificial or natural adsorbent, where they can be properly disposed off or retrieved [15].

Silicate clay, a naturally occurring nanoparticle adsorbent produced by silicate weathering on the earth's surface, is present in deposits totaling more than 50 million tons worldwide. Owing to its negatively charged surface, large specific surface area, robust cation exchange, and chemical

✉ Marwa A. Eid
Marwa_eid1@yahoo.com

1 Analytical Chemistry and Control Department, Hot Laboratories and Waste Management Center, Egyptian Atomic Energy Authority, Cairo, Egypt

2 Radioactive Waste Management Unit, Hot Laboratories and Waste Management Center, Egyptian Atomic Energy Authority, Cairo, Egypt

3 Nuclear Fuel Chemistry Department, Hot Laboratories and Waste Management Center, Egyptian Atomic Energy Authority, Cairo, Egypt

4 Radiation Protection Department and Safety, Hot Laboratories and Waste Management Center, Egyptian Atomic Energy Authority, Cairo, Egypt

5 Nuclear Fuel Technology Department, Hot Laboratories and Waste Management Center, Egyptian Atomic Energy Authority, Cairo, Egypt

pollution-free properties, clay minerals have become one of the most studied activations, modification, and functionalization topics among many scientists [16].

A typical silicate clay mineral with significant deposits and high magnesium content is talc (T) having the chemical formula of $Mg_3Si_4O_{10}(OH)_2$. Talc is distinguished by its 2:1 sheets structure, which consists of a layer of $Mg(OH)_2$ and two layers of the Si–O tetrahedron [17]. After being broken up into talc powder and processed, the talc powder is separated. It is widely used in a variety of industries, including ceramics, paper, plastic, rubber, food, medicine, and food processing [18]. Talc's high porosity, substantial specific surface area, rod-like structure, and the profusion of hydrophilic Si–OH make it an excellent adsorbent for the decontamination of radioactive wastewater [19–21]. Talc composites have been enhanced with other substances including P(AA-AN)-talc [17], Fe_3O_4/Talc [22], and modified talcum [23]. Investigators haven't looked into the impregnation of talc layers with iron ions or phosphate groups. In this study, iron phosphate@talc (IPT) was developed as a novel substance and used to filter out ^{137}Cs, $^{152+154}Eu$, and ^{131}Ba from radioactive wastewater. Using sorption techniques, the sorption efficiency (% S.E.) of ^{137}Cs, $^{152+154}Eu$, and ^{131}Ba from liquid waste was investigated [24, 25].

The purpose of this research is to reduce the negative effects of ^{137}Cs, $^{152+154}Eu$, and ^{131}Ba by applying the sorption technique to IPT sorbent prepared by the precipitation method. Fourier-transform infrared spectroscopy (FT-IR), scanning electron microscopy (SEM), X-ray diffraction (XRD), and X-ray fluorescence (XRF) were used as analytical techniques to characterize IPT sorbent. Batch experiments were used to calculate the optimal sorption parameters for ^{137}Cs, $^{152+154}Eu$, and ^{131}Ba, which include time, pH, temperature, and initial metal concentration.

Experimental

Materials

The suppliers of $BaCl_2$ and $FeCl_3$ are Loba Chemie (India), KH_2PO_4 Alpha Chemika (India), $Na_5P_3O_{10}$ Goway (China), and HNO_3 Merck (Germany). NaOH, NH_3, and NaCl El-Nasr Company (Egypt). For all works, double-distilled water (DDW) was used. The reagents employed in this study were of the analytical grade without any further purification.

Radioisotopes tracers

Radioactive tracers ^{131}Ba and $^{152+154}Eu$ were obtained via the activation reaction of (n, γ) by neutron irradiation of 0.05 g weight of metal chloride salts wrapped in double aluminum foil and goes to the vertical irradiation channels inside the core of the second Egyptian Training Research Reactor ETRR-2 for 3 h at a neutron flux of 1×10^{14} n cm^{-2} s^{-1} to obtain the desired radioactivity level. Then, they were left to cool for a week before dissolving and counting using the gamma spectrometry technique, to allow all undesirable short-lived radionuclides to decay. ^{137}Cs was obtained from a standard radioactive solution purchased from Eckert and Ziegler company with an initial activity of 3.7×10^6 Bq (≈ 100 μCi).

Preparation

For the preparation of talc (T), talc phosphate (TP), and iron phosphate@talc (IPT) sorbents, a simple and ambient precipitation procedure was used through the final stage.

(i) Preparation of talc solution by addition of 7.5 g $Na_5P_3O_{10}$ as dispersing agent to 75 g talc powder with the addition of DDW to reach 750 mL with constant stirring for 120 min.
(ii) Preparation of 0.2 M KH_2PO_4 and 0.2 M $FeCl_3$ solutions by dissolving 14.2 g KH_2PO_4 with 500 mL DDW and 8.11 g $FeCl_3$ with 250 mL DDW.
(iii) Different ratios of the equimolar solutions from $FeCl_3$ and KH_2PO_4 were added to the talc solution as the following (0:0:1, 1:0:1, 1:1:1) respectively, details are listed in Table 1.

Adding the prepared solutions together and stirring consistently for 2 h, adding 10% NH_4OH solution to the mixture, as observed a color gel began to form at a pH of 7.5. The formed gel was left undisturbed overnight before being washed with DDW, dried at 60 ± 1 °C, and finally ground to get a fine powder.

Table 1 Conditions for the synthesis of T, TP, and IPT sorbents and % S.E. of ^{137}Cs, $^{152+154}Eu$, and ^{131}Ba [$C_i = 50$ mg L^{-1}, V/m = 0.1 L g^{-1}, and shaking time 24 h]

Sorbents	$FeCl_3$, [mL]	KH_2PO_4, [mL]	Talc, [mL]	^{131}Ba		^{137}Cs		$^{152+154}Eu$	
				pH	% S.E	pH	% S.E	pH	% S.E
T	0	0	250	6.0	66.5	6.0	49.85	4.0	41.8
TP	0	250	250		75.31		61.2		56.6
IPT	250	250	250		96.22		83.1		80.9

Preliminary studies for sorbents selection

To perform the measurements, 5 mL each of radioactive solutions of ^{137}Cs, $^{152+154}$Eu, and ^{131}Ba were added to 0.05 g of three different prepared samples and shaken at 298 ± 1 K in a thermostat shaker (Kottermann D-1362, Germany). The solution and the solid are decanted as soon as the shaker is turned off after 24 h.

The activities of ^{137}Cs, $^{152+154}$Eu, and ^{131}Ba were measured for 3600 s using a coaxial p-type HPGe detector (GEM-series, ORTEC, USA) connected to a multichannel analyzer system (MCA, Inspector 2000 Series, Canberra, USA). The % sorption efficiency (% S.E.) can be computed by using Eq. (1) [26, 27];

$$\%\ \text{S.E.} = \left(\frac{A_i - A_f}{A_i}\right)100 \tag{1}$$

A_i and A_f are the initial and final activity of ^{137}Cs, $^{152+154}$Eu, and ^{131}Ba, respectively.

Instruments for sorbent characterization

Germany's Bruker XRD diffractometer D2 Phaser II was used to examine the crystal structure of the IPT sorbent. FT-IR measurements were made in the wavenumber range of 4000–400 cm^{-1} using an automated spectrophotometer Alpha II Bruker (Germany). The Philips sequential X-ray spectrometer-2400 was used to identify the elemental composition of IPT sorbent. Using the Super-Q quantitative application program, the percentages of Mg, Al, Si, P, Ca, K, and Fe were estimated. SEM JSM-6510A Model (Japan) was used to study the surface morphology of the IPT sorbent material.

Chemical stability

Different solvents such as (DDW, ethanol, methyl ethyl ketone, HNO_3, and NaOH) were used to study the solubility percentage of the IPT by constant shaking 0.1 g of solid and 10 mL of studied solvents for 3 days at 25 ± 1 °C. The amount of IPT sorbent left in the solution was measured gravimetrically by decantation of filtrate and then dried [24, 28].

pH titration

IPT sorbent was examined using the Topp and Pepper method to detect pH titration by the NaOH–NaCl system [29]. Each 10.0 mL of NaOH (0.1 M)–NaCl (0.1 M) mixed by different volumetric ratios was contacted with 0.1 g of the prepared sorbent and then constantly stirred. After a standard 24 h interval, the pH of the solutions was recorded using a pH meter.

Sorption experimentation

All equilibrium measurements were carried out by shaking 0.05 g of IPT sorbent with 5.0 mL of ^{137}Cs, $^{152+154}$Eu, and ^{131}Ba at a baseline concentration of 50 mg L^{-1} in a shaker thermostat model Kottermann D-1362 (Germany), and V/m = 100 mL g^{-1}. The variation in sorption parameters such as pH (1–7), metal concentrations (50–500 mg L^{-1}), temperatures (30, 45, and 60 °C), and contacting time (5–300 min) were checked to get the optimum sorption conditions. IPT sorbent batch-wise interacted with ^{137}Cs, $^{152+154}$Eu, and ^{131}Ba. Following sorption, the samples were separated by filtration. The amount sorbed q_e was calculated using the following equation [30–32]:

$$q_e(\text{mg g}^{-1}) = \left(\frac{A_i - A_e}{A_i}\right)\left(\frac{C_i V}{m}\right) \tag{2}$$

A_e, V, C_i, and m are the activity of a solution at equilibrium, the solution volume (L), initial concentration, and the IPT weight (g), respectively. The distribution coefficients K_d and separation factors α_B^A as a function of pH were determined with the subsequent equations [31, 33–35]:

$$K_d(\text{mL g}^{-1}) = \left(\frac{A_i - A_f}{A_f}\right)\left(\frac{V}{m}\right) \tag{3}$$

and

$$\alpha_B^A = \frac{K_d(A)}{K_d(B)} \tag{4}$$

V is the volume of ^{137}Cs, $^{152+154}$Eu, and ^{131}Ba (mL). K_d(A), and K_d(B) are the distribution coefficients for the two competing species A and B in the system.

Results and discussion

Preliminary studies

The sorption efficiency (% S.E.) of the studied radiotracer either onto talc, TP, and IPT sorbents is presented in Table 1. These results prove that an enhancement was attained in the sorption behavior of ^{137}Cs, $^{152+154}$Eu, and

^{131}Ba onto IPT sorbent than T and TP sorbents. So, IPT sorbent was used for all experiments.

XRD analysis

XRD was utilized to indicate the degree of crystallinity of IPT sorbent as presented in Fig. 1a. Figure 1a reveals that IPT sorbent has a uniform hexagonal crystalline nature and demonstrates the existence of characteristic peaks of talc addressed at 2θ values (8.33°, 14.46°, 16.71°, 19.86°, 24.65°, 25.18°, 28.69°, 35.35°, 36.45°, 39.4°, 42.6°, 45.22°, 55.1°, 58.12°, 60.45°, 66.3°, 67.99°, 73.3°, and 79.3°) related to Miller indices of hkl values (100, 2–10, 200, 101, 201, 300, 3–21, 4–31, 002, 2–12, 500, 302, 601, 2–13, 8–40, 8–61, 403, 8–52, and 2–14) respectively. Peaks of iron and phosphorus are significantly appeared at 2θ values (10.82°, 11.96°, 14.92°, 22.93°, 58.66°, and 67.24°). Moreover, some impurities are detected from Ca, Al, and K at 2θ values (9.57°, 12.61°, 18.91°, 19.54°, 25.19°, 26.79°, 28.02°, 28.75°, 34.72°, 35.37°, 36.79°, 55.31°, 60.18°, 61.60°, and 79.42°). This result gives a good estimation of the existence of iron and phosphorus in the present work-prepared IPT sorbent [36].

FT-IR spectrum

FT-IR analysis of IPT sorbent was existing in Fig. 1b. It is clear that from this Figure eight bands appeared in IPT sorbent at wavenumbers (3749, 3621, 1630, 1049, 941, 873, 745, and 577 cm^{-1}). The bands at 3621 and 947 cm^{-1} are due to A1–A1–OH (stretching and bending vibration, respectively) [37, 38]. The band at 3749 cm^{-1} is related to Al–OH–Mg bonds present in talc powder [39]. The bands at 3621 and 1639 cm^{-1} agreed to OH frequencies of the H_2O molecule (stretching and bending) respectively [24] or officially to P–OH [40, 41]. At the same time, bands at (1049, 873, and 745 cm^{-1}) are due to Si–O, Si–O–Al, and Si–O–Mg bending, respectively [37]. Bands from 941 and 577 cm^{-1} are related to M–O (where M is Al or Fe) [40]. The FT-IR analysis of IPT sorbent loaded by Cs(I), Ba(II), and Eu(III) ions presented in Fig. 1b has the same bands observed in the FT-IR of IPT sorbent. The band at 577 cm^{-1} shifted to 640 cm^{-1} for IPT loaded by Cs(I), shifted to 586 cm^{-1} for IPT loaded by Ba(II), and shifted to 660 cm^{-1} for IPT loaded by Eu(III). Whereas the intensity of bands at 3621 and 1630 cm^{-1} was increased after loading of IPT sorbent with Cs(I), Ba(II), and Eu(III) ions. These data confirmed that the combination between Cs(I), Ba(II), and Eu(III) ions with IPT sorbent was achieved.

SEM analysis

SEM images of the proposed sorbent material are shown in Fig. 2 at different magnification powers of X500, X1000, and X2000. Results show a heterogeneous distribution of the iron and phosphate particles (white color) on the talc

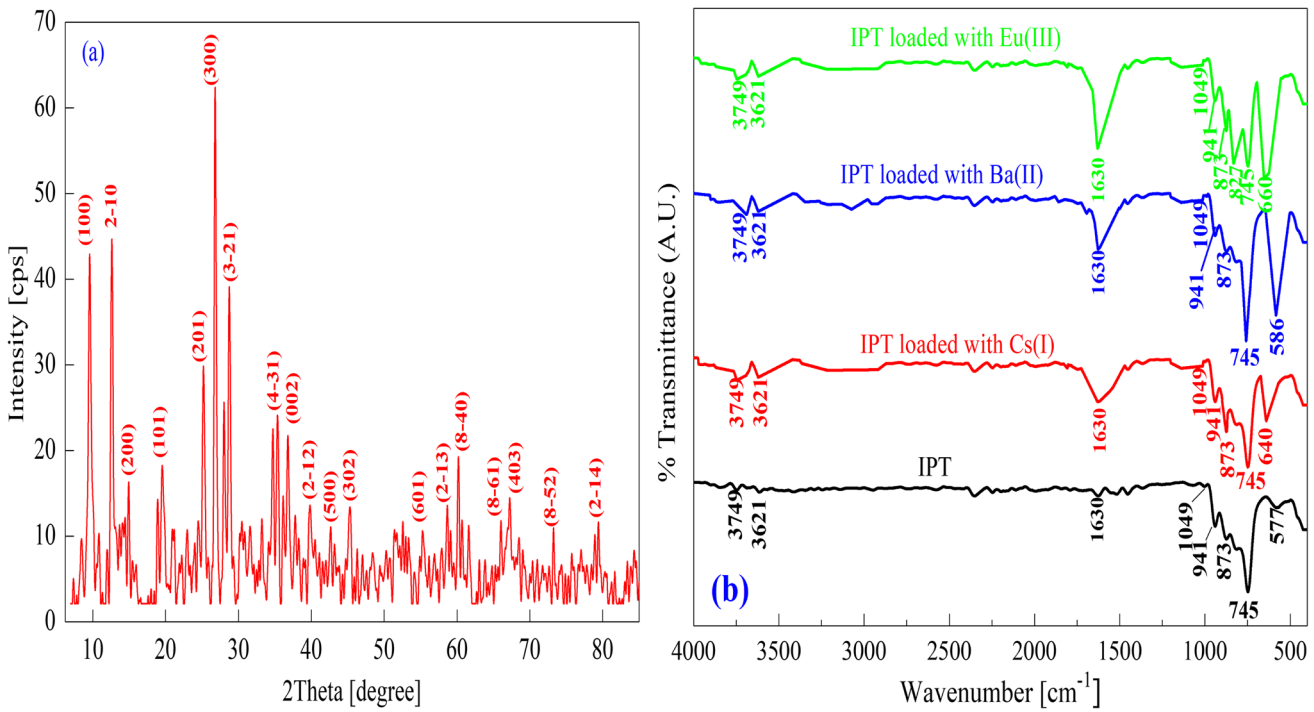

Fig. 1 **a** XRD pattern and **b** FT-IR spectrum of IPT sorbent

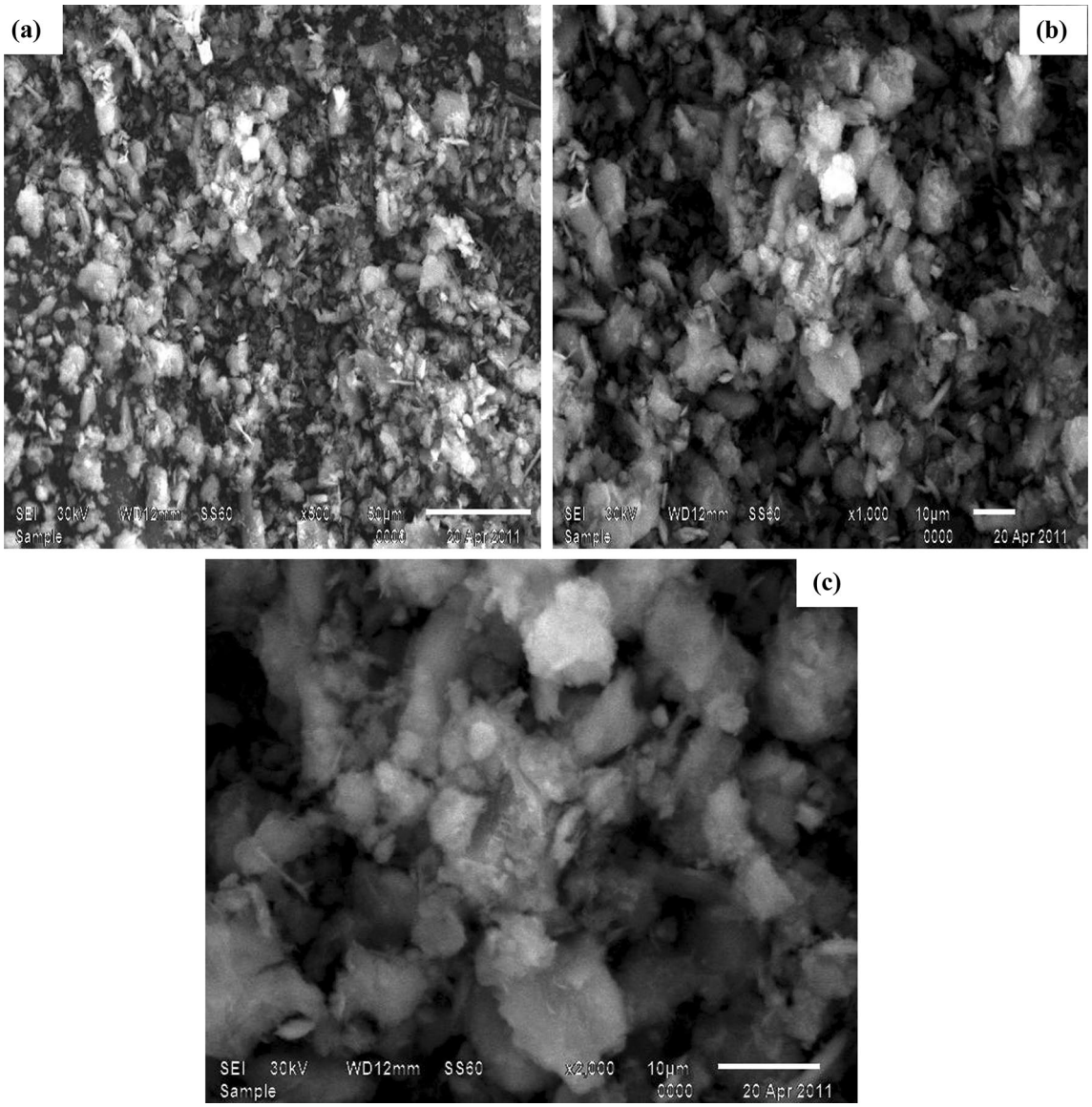

Fig. 2 SEM images for the proposed IPT sorbent material at different magnification powers **a** X500 **b** X1000 **c** X2000

media (grey color), simply they are similar to a bulk of tiny islands on the ocean surface. At small magnification power of X500, the surface appears to have very small porous, and by increasing the magnification power at X1000 and X2000, these particles are rugged, and sharp and have intermolecular distances that support the physical sorption process on the material.

XRF analysis

The percentage of metal present in IPT sorbent based on an X-ray fluorescence spectrometer was measured and revealed that the prepared IPT sorbent possesses the values 14.2, 4.31, 24.26, 15.11, 3.92, 3.38, and 34.82 for Mg, Al, Si, P, Ca, K, and Fe respectively. These data confirmed that the main constituents are Fe, Si, P, and Mg. Also, the reason for the appearance of Ca, K, and Al elements in XRF analysis is due to the presence of these elements in natural talc.

pH titration curve

Figure 3 displays the pH titration curve of IPT sorbent. The X-axis and Y-axis characterize the number of mL of NaOH solution interacting with 0.1 g of IPT sorbent, and the pH of the effluent, respectively. The pH titration curve for IPT

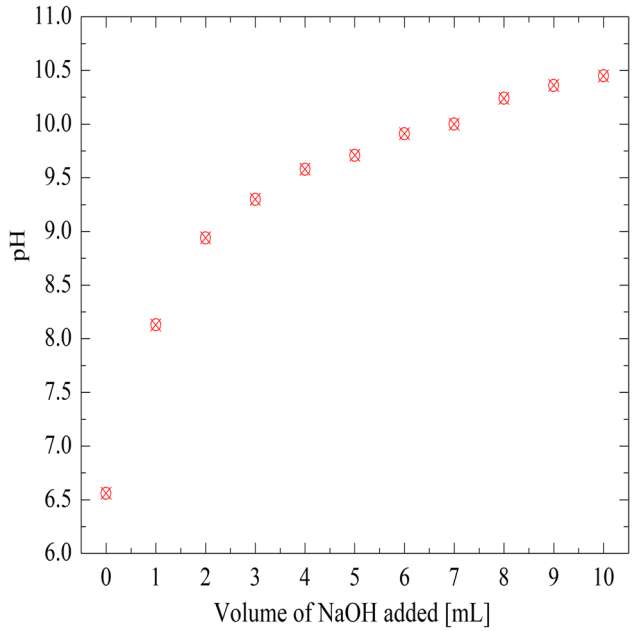

Fig. 3 pH titration curve of IPT sorbent

sorbent reflect only one inflection point at a pH value equal 10, revealing that it is a mono-functional sorbent. This is the same behavior as ZrSnP prepared by Abass et al. [24].

Chemical stability

The solubility test of the IPT sorbent is represented in Table 2 reflecting that the prepared sorbent was stable in DDW, ethanol, methyl ethyl ketone, HNO_3, and NaOH below 2 mol L^{-1}. Table 2 exhibits that IPT sorbent has relatively high stability to chemical reagents compared to other sorbents [42–44].

Table 2 Chemical stability of IPT sorbent in different solvents

Solvents	% Solubility
DDW	Below detection limit
Ethanol, [96%]	0.5
Methyl ethyl ketone	2.25
0.5 mol/L HNO_3	2.12
1 mol/L HNO_3	2.93
3 mol/L HNO_3	5.56
0.5 mol/L NaOH	4.23
2 mol/L NaOH	24.62

Sorption studies

Influence of pH on the sorption efficiency and distribution coefficients (K_d)

The sorption of ^{137}Cs, $^{152+154}$Eu, and ^{131}Ba onto IPT sorbent in different pH values was studied from aqueous media as exposed in Fig. 4a. According to this Figure, the % S.E. increases with increasing pH until it reaches the maximum levels of 96.0, 83.2, and 81.0% for ^{131}Ba, ^{137}Cs, and ^{152}Eu, respectively, at pH 6 for ^{131}Ba and ^{137}Cs and pH 4 for $^{152+154}$Eu. The sorption of ^{131}Ba, ^{137}Cs, and ^{152}Eu was found to be low at low pH values, which is likely caused by the protonation of the surface-active sites and the rise in H_3O^+ ions in the aqueous solution [45]. As a result of competition for the accessible binding surface active site produced by the positively charged surface sites, uptakes of the radionuclides ^{131}Ba, ^{137}Cs, and ^{152}Eu were reduced. With rising pH values, the concentration of H_3O^+ ions is reduced while the concentration of OH^- is raised which causes deprotonation of the sorbent surface, such explanations mean that the surface of the IPT sorbent tends to have a negative charge. Hence, the attraction among the surface of IPT and the positive charge of ^{131}Ba, ^{137}Cs, and ^{152}Eu in the solution was improved.

The speciation of Ba(II), Cs(I), and Eu(III) ions in a liquid solution at different pH values (1- 7), at ionic strength 0.001 M and 25 °C was performed using the MEDUSA program which gives information about the distribution of species as a function of pH [46], as exposed in Fig. 4b–d. The results showed that the speciation of Cs(I) and Ba(II) ions have no precipitate at all pHs (1–7) [7]. H^+ ions concentration was decreased with increasing pH values and at pH approximately 7, H^+ ions disappeared and at pH 5, OH^- ions start to increase with increasing pH values. The speciation of Eu(III) ions has no precipitate at a pH range from 1 to 2.2 with no presence of these ions in the hydroxide form. The hydrolysis of Eu(III) ions begins at a pH value above 2.2, and different species can be shaped, such as $EuOH^{2+}$ and $Eu(OH)_2^+$ formed at pH 5, the uptake of Eu(III) increases with pH until 4.0 and then decreased due to formation of $EuOH^{2+}$ and $Eu(OH)_2^+$. After pH 6 Eu(III) precipitated as $Eu(OH)_3$. The above data of chemical speciation are compatible with the sorption of ^{137}Cs, $^{152+154}$Eu, and ^{131}Ba onto IPT sorbent at pH 6 for ^{131}Ba and ^{137}Cs and pH 4 for $^{152+154}$Eu.

Distribution coefficients (K_d) and separation factors $\left(\alpha_B^A\right)$ at different pHs (1–7) were calculated and tabulated in Table 3 and reflected that K_d has the affinity order: ^{131}Ba > ^{137}Cs > $^{152+154}$Eu, this result supports that ^{131}Ba and ^{137}Cs uptake was carried out in the case of ionic radii [^{131}Ba and ^{137}Cs have ionic radius 0.142 and 0.165 nm, respectively] whereas the sorption of and $^{152+154}$Eu was done as hydrated ionic radius [$^{152+154}$Eu has an ionic radius

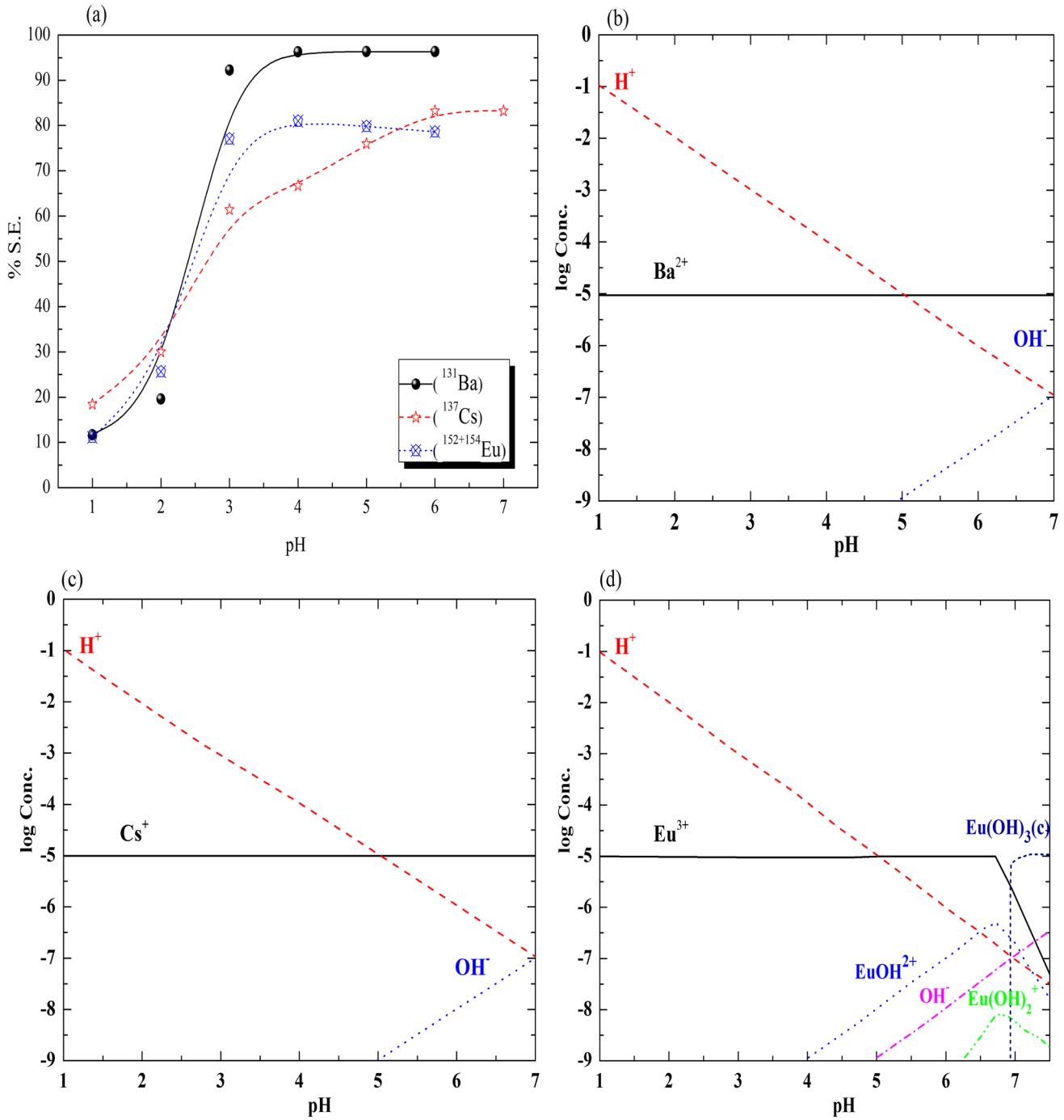

Fig. 4 **a** Effect of pH on the % S.E. of ^{137}Cs, $^{152+154}$Eu, and ^{131}Ba onto IPT sorbent and chemical speciation of **b** Ba(II), **c** Cs(I), and **d** Eu(III) at pH range (1–7), ionic strength 0.001, and 25 °C

0.107 nm]. Radionuclides with lower ionic radius (^{131}Ba) easily enter the cavities of IPT sorbent increasing in sorption and consequently increasing K_d [47, 48]. Separation factors for studied radionuclides reflected that ^{131}Ba has a good separation factor at different pH values. Also, the data obtained in Table 3 reveal that the best separation factors for studied radionuclides were at pH 4 (6.1 for the separation of ^{131}Ba from $^{152+154}$Eu and 12.9 for the separation of ^{131}Ba from ^{137}Cs).

Nonlinear relationships between log K_d and pH were observed for the studied radionuclides, as shown in Fig. 5a. This relationship reveals the exchange reaction is

Table 3 Distribution coefficients and separation factors of ^{137}Cs, $^{152+154}$Eu, and ^{131}Ba onto IPT sorbent at 25 ± 1 °C

pH	K_d [mL g^{-1}] and α_B^A	$^{152+154}$Eu	^{137}Cs	^{131}Ba
1	K_d	12.6	22.6	13.3
	α_B^A		1.8	1.1
				0.6
2	K_d	34.5	42.9	24.4
	α_B^A		1.2	0.7
				0.6
3	K_d	335.7	159.4	1190.8
	α_B^A		0.5	3.5
				7.5
4	K_d	425.5	200.5	2581.6
	α_B^A		0.5	6.1
				12.9
5	K_d	–	316.0	2636.0
	α_B^A		–	–
				8.3
6	K_d	–	496.7	2637.0
	α_B^A –		–	
				5.3

non-ideal. The difference could be attributed to the prominence of a mechanism other than ion exchange, such as precipitation and/or surface adsorption [33].

Shaking time impact

The impact of contact time on ^{137}Cs, $^{152+154}$Eu, and ^{131}Ba sorption onto IPT sorbent was studied at a fixed temperature (298 ± 1 K), initial concentration C_i = 50 mg L^{-1}, V/m = 0.1 L g^{-1}, shaking time (5 min–24 h), pH = 4 for $^{152+154}$Eu, and pH = 6 for ^{131}Ba and ^{137}Cs, and the data are shown in Fig. 5b. This Figure examined that the sorption of ^{137}Cs, $^{152+154}$Eu, and ^{131}Ba onto IPT sorbent enhanced with contact time attain equilibrium at 1 h for ^{137}Cs and $^{152+154}$Eu and 5 h for ^{131}Ba. The rate of ^{137}Cs and $^{152+154}$Eu uptake onto IPT sorbent rapidly increases with time from 5 to 60 min reaching flattened behavior. Moreover, the rate ^{131}Ba uptake is different, it takes two stages to be flattened the first one start 5–90 min and then form rapidly rises from 150 to 300 min, and starts to flatten again till 1000 min achieving the maximum % S.E. Results can be concluded as there is no significant change of the uptake above 100 min for ^{137}Cs and $^{152+154}$Eu but at 300 min for ^{131}Ba.

Kinetic studies

In the present work, pseudo-1st-order (Lagergren equation), and pseudo-2nd-order were applied to study and analyze the

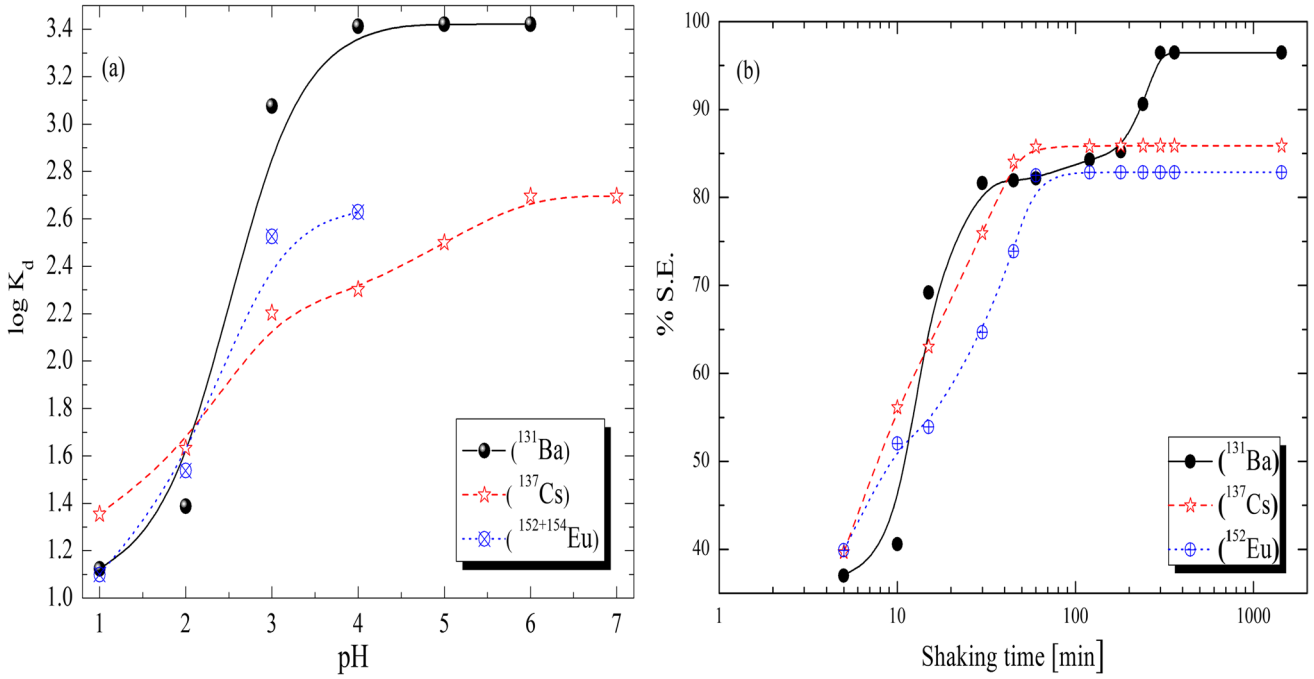

Fig. 5 Sorption of ^{137}Cs, $^{152+154}$Eu, and ^{131}Ba onto IPT sorbent, **a** plots of log K_d against pH at 25 ± 1 °C and **b** effect of shaking time on the % S.E

obtained data from the sorption of ^{137}Cs, $^{152+154}$Eu, and ^{131}Ba onto IPT sorbent, their equations are given below as [49, 50]:

$$\log (q_e - q_t) = \log\ q_e - \frac{K_f t}{2.303} \quad (5)$$

$$\frac{t}{q_t} = \frac{1}{K_s q_e^2} + \frac{t}{q_e} \quad (6)$$

in which, q_t is the value of the amount sorbed per unit mass (mg g^{-1}) at time t, K_f (min^{-1}), and K_s (g mg^{-1} min^{-1}) are the rate constants of two kinetic equations. By plotting log ($q_e - q_t$) versus t and t/q_t versus t, the obtained results are displayed in Fig. 6a and b. The result shows that the obtained experimental data are well-fitted with the pseudo-2nd-order model rather than the 1st-order model. The calculated constants of the two models are tabulated in Table 4. By comparing the model data with the obtained experimental data; it

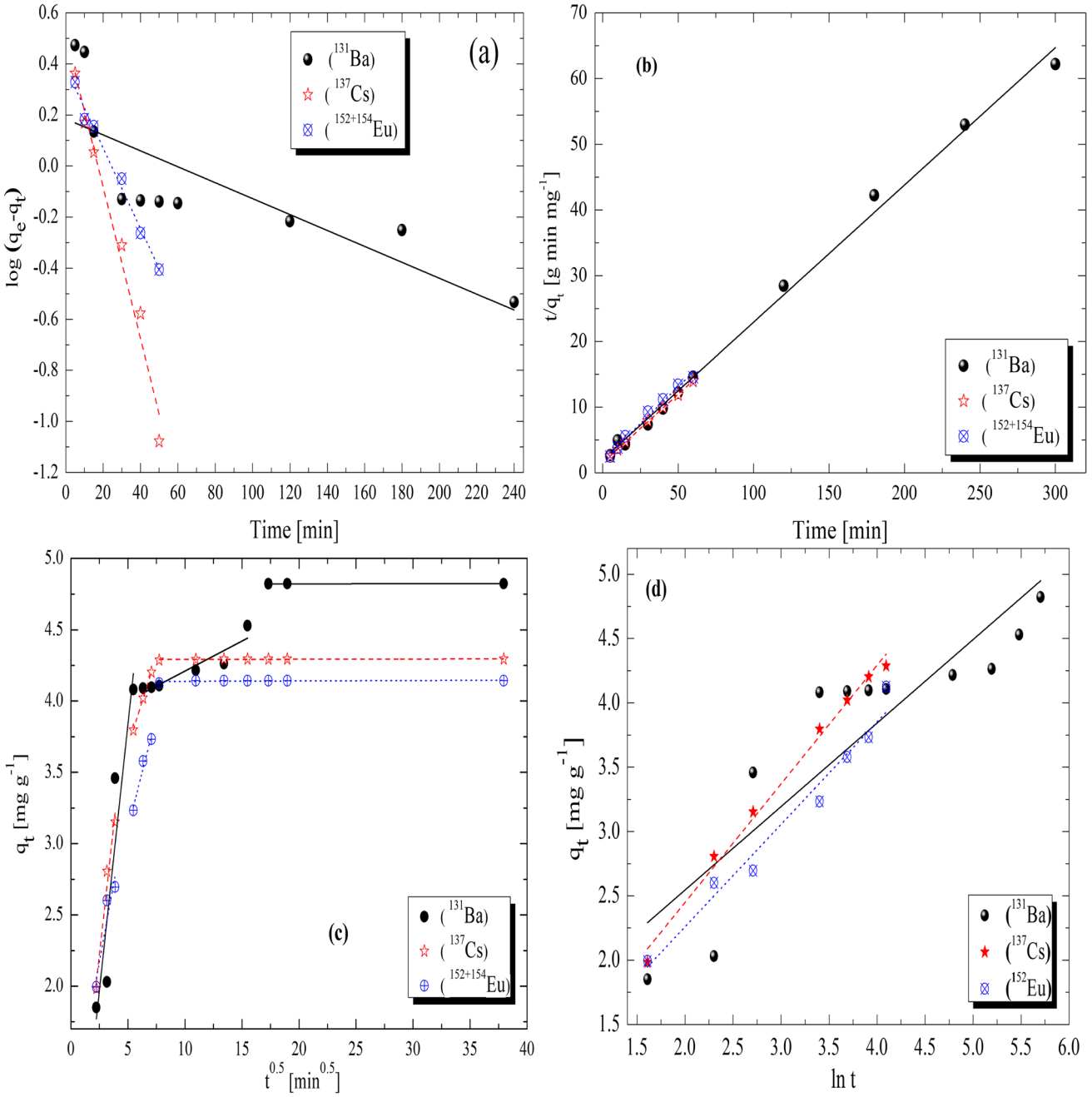

Fig. 6 Kinetic modeling fitting of ^{137}Cs, $^{152+154}$Eu, and ^{131}Ba onto IPT sorbent, **a** pseudo-1st-order kinetic, **b** pseudo-2nd-order kinetic, **c** intra-particle diffusion, and **d** Elovich models at 25 ± 1 °C

Table 4 Kinetic parameters and correlation coefficients (R^2) for pseudo-1st-order, pseudo-2nd-order, intra-particle diffusion, and Elovich models for the sorption of ^{137}Cs, $^{152+154}$Eu, and ^{131}Ba onto IPT sorbent at 25 ± 1 °C

Radionuclides	q_e (exp) [mg g^{-1}]	Pseudo-1st-order			Pseudo-2nd-order			
		q_e (cal) [mg g^{-1}]	K_f	R^2	q_e (cal) [mg g^{-1}]	h	K_s	R^2
^{131}Ba	4.82	1.53	−0.003	0.580	4.79	0.49	0.089	0.995
^{137}Cs	4.29	3.25	−0.030	0.976	4.81	1.55	0.028	1.000
$^{152+154}$Eu	4.14	2.43	−0.016	0.987	4.47	1.90	0.026	0.985

Intra-particle diffusion					Elovich		
Radionuclides	Time range [min]	K_{id}	C	R^2	α	β	R^2
^{131}Ba	5–30	0.747	0.101	0.822	4.43	1.541	0.777
	40–240	0.04209	3.69273	0.7626			
	300–1440	–	4.824	–			
^{137}Cs	5–15	0.72235	0.41523	0.9516	1.77	1.084	0.965
	30–50	0.25484	2.40406	0.9987			
	60–1440	–	4.29077	–			
$^{152+154}$Eu	5–15	0.43951	1.0719	0.7983	1.84	1.255	0.967
	30–50	0.31534	1.53129	0.9345			
	60–1440	–	4.13563	–			

proposes that pseudo-2nd-order sorption is the main mechanism, as data quality is related to R^2 (a goodness-of-fit measure for linear regression models); for ^{137}Cs, $^{152+154}$Eu, and ^{131}Ba are almost equal to one compared with its low values obtained from the pseudo-1st-order kinetic model. Also, the values of q_e calculated from the pseudo-2nd-order model were nearer to the values of q_e (experimental). This means the adsorption of ^{137}Cs, $^{152+154}$Eu, and ^{131}Ba was found to be a chemisorption process [51, 52].

The diffusion mechanism of ^{137}Cs, $^{152+154}$Eu, and ^{131}Ba onto IPT sorbent was investigated by the intra-particle diffusion model which is presented in the next equation [53, 54].

$$q_t = K_{id} t^{0.5} + C \tag{7}$$

Which, K_{id} and C are the intra-particle diffusion rate constant (mg g^{-1} $min^{-0.5}$) and the intra-particle diffusion constant which is directly proportional to the boundary layer thickness, respectively. The plot of q_t versus $t^{0.5}$ is assumed in Fig. 6c. The value of the rate parameter was calculated from the slope, and the value of R^2 is assumed in Table 4. Three steps were used to create the intra-particle diffusion model for ^{137}Cs, $^{152+154}$Eu, and ^{131}Ba sorption [55, 56]. (a) The diffusion of ^{137}Cs, $^{152+154}$Eu, and ^{131}Ba from the solution to the surface of the IPT sorbent (from 5 to 30 min) for ^{131}Ba and (from 5 to 15 min) for ^{137}Cs and $^{152+154}$Eu. (b) The gradual sorption on the surface of the IPT sorbent, which may be the rate-limiting step (from 40 to 240 min) for ^{131}Ba, (from 30 to 50 min) for ^{137}Cs and $^{152+154}$Eu. (c) The equilibrium saturation (from 300 to 1440 min) for ^{131}Ba and (from 60 to 1440 min) for ^{137}Cs and $^{152+154}$Eu. The sorption mechanism of ^{137}Cs, $^{152+154}$Eu, and ^{131}Ba onto IPT sorbent was found to be fast at the initial period of contact time and then to become constant with the increase in time. The sorption mechanism, which comprises both film and intra-particle diffusion, is primarily controlled by the multi-diffusion step.

The Elovich kinetic model is used to describe the kinetics of chemisorption on highly energetically heterogeneous solid surfaces. The mathematical linear form of this model is expressed as [57]:

$$q_t = \frac{1}{\beta}\ln(\alpha\beta) + \frac{1}{\beta}\ln t \tag{8}$$

where: α is the Elovich coefficient which represents the initial sorption rate (mg g^{-1} min^{-1}) and β is a parameter related to the desorption constant (g mg^{-1}) during any experiment. The plots of q_t vs. ln t for the sorption of ^{137}Cs, $^{152+154}$Eu, and ^{131}Ba onto IPT sorbent are shown in Fig. 6d. It gives a linear relationship with a slope of 1/β and an intercept of 1/β ln(αβ). The values of Elovich prediction model parameters were determined from the obtained linear form and listed in Table 4. The data in Table 4 declared that the Elovich equation did not fit the experimental results based on the low values of R^2. This validated the inapplicability of this model for describing the sorption of ^{137}Cs, $^{152+154}$Eu, and ^{131}Ba onto IPT sorbent.

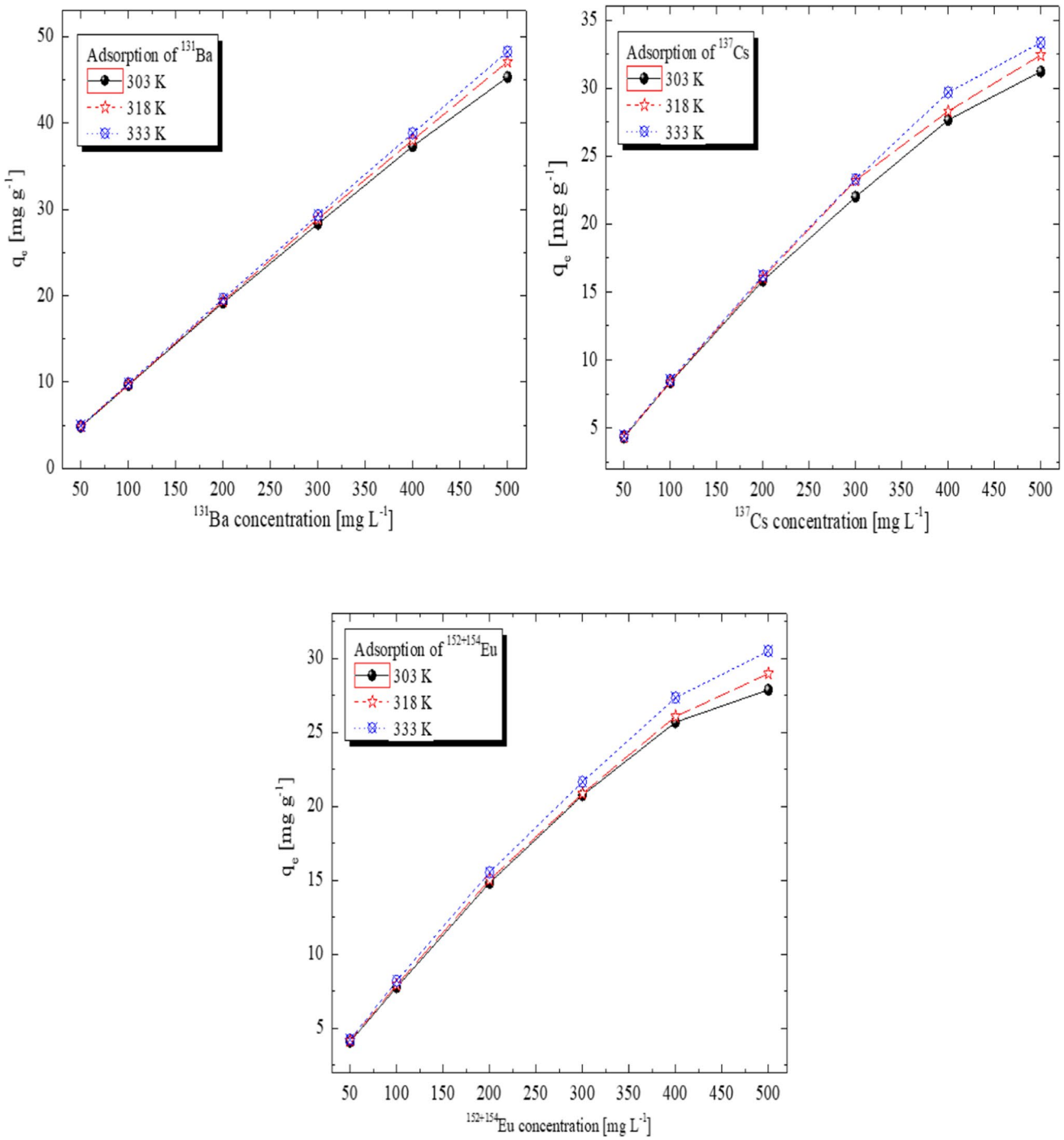

Fig. 7 Effect of initial concentration of ^{137}Cs, $^{152+154}$Eu, and ^{131}Ba onto IPT sorbent at different temperatures [V/m = 0.1 L g^{-1}, pH = 6 for ^{131}Ba and ^{137}Cs and pH = 4 for.$^{152+154}$Eu]

Effect of concentrations

Figure 7 reveals the plots between q_e of ^{137}Cs, $^{152+154}$Eu, and ^{131}Ba onto IPT and C_i at the range (50–500 mg L^{-1}) at different reaction temperatures. The q_e of ^{137}Cs, $^{152+154}$Eu, and ^{131}Ba onto IPT sorbent rises as the initial concentration of ^{137}Cs, $^{152+154}$Eu, and ^{131}Ba increases. As well as, the q_e increases by increasing reaction temperature indicating the endothermic nature of the sorption.

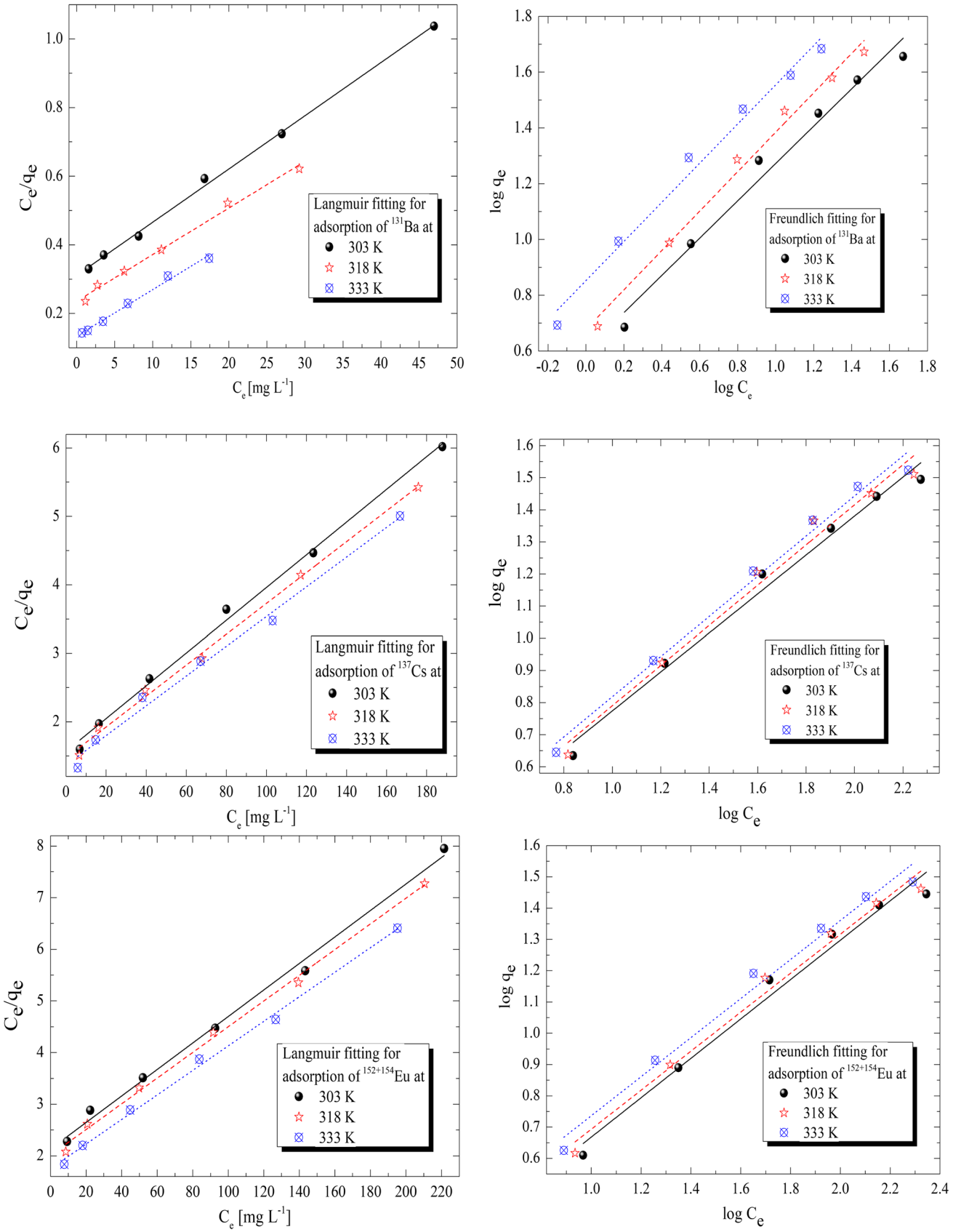

Fig. 8 Isothermal modeling fitting of ^{137}Cs, $^{152+154}$Eu, and ^{131}Ba onto IPT sorbent at different reaction temperatures [V/m = 0.1 L g^{-1}, pH = 6 for ^{131}Ba and ^{137}Cs and pH = 4 for.$^{152+154}$Eu]

Isothermal modeling

The Langmuir isotherm model can be represented in the equation [3, 58]:

$$\frac{C_e}{q_e} = \frac{C_e}{Q_{max}} + \frac{1}{bQ_{max}} \quad (9)$$

Q_{max} and b are the theoretical monolayer capacity (mg g^{-1}) and the sorption equilibrium constant is related to the energy of sorption, respectively, and C_e is the equilibrium concentration. As shown in Fig. 8, plotting C_e/q_e and C_e gives straight lines for ^{137}Cs, $^{152+154}$Eu, and ^{131}Ba onto IPT sorbent at temperatures (303, 318, and 333 K). The calculated data from the slopes and intercepts of the linear form of the Langmuir model for ^{137}Cs, $^{152+154}$Eu, and ^{131}Ba sorption onto IPT sorbent at 303, 318, and 333 K were presented in Table 5. The R^2 values confirm that the high applicability of Langmuir isotherm for the sorption of these radionuclides onto IPT sorbent. The Q_{max} was (64.47, 73.64, and 73.75 mg g^{-1}), (41.1, 44.37, and 46.06 mg g^{-1}), and (39.0, 40.2, and 42.11 mg g^{-1}) for ^{131}Ba, ^{137}Cs, and $^{152+154}$Eu at 303, 318, and 333 K, respectively. These data prove the endothermic nature of the sorption of ^{137}Cs, $^{152+154}$Eu, and ^{131}Ba onto IPT sorbent because of rising Q_{max} for ^{131}Ba, ^{137}Cs, and $^{152+154}$Eu with increasing reaction temperature.

The equilibrium parameter (R_L) can be obtained from the Langmuir constant b as follows:

$$R_L = \frac{1}{1 + bC_i} \quad (10)$$

The R_L values reflect the type of isotherm to be irreversible if, $R_L = 0$, favorable $0 < R_L < 1$, linear if $R_L = 1$, or unfavorable $R_L > 1$. Table 5 proves that the $0 < R_L < 1$ reveals the favorable sorption isotherms of studied radionuclides [3].

A linear form of Freundlich expression can be represented as:

$$\log\ q_e = \log\ K_F + \frac{1}{n} \log\ C_e \quad (11)$$

In which, K_F and 1/n are the Freundlich constant and heterogeneity factors. It represents the amount of ^{137}Cs, $^{152+154}$Eu, and ^{131}Ba onto IPT for unit equilibrium concentration. The values of 1/n signify the deviation from the linearity of sorption as follows: (i) $1/n = 1$ reflects that the sorption is linear; (ii) $1/n < 1$ implies heterogeneous surface structure with minimum interaction between the adsorbed atoms, and (iii) $1/n > 1$ implies homogeneous surface

Table 5 Isotherm parameters for sorption of ^{137}Cs, $^{152+154}$Eu, and ^{131}Ba onto IPT sorbent at different reaction temperatures

Radionuclides	Temp [K]	Langmuir constants				Freundlich constants		
		Q_{max} [mg g^{-1}]	b [L mg^{-1}]	R_L	R^2	1/n	K_F [mg g^{-1}]	R^2
^{131}Ba	303	64.47	0.050	0.04	0.998	0.67	4.02	0.976
	318	73.64	0.058	0.03	0.991	0.71	4.77	0.988
	333	73.75	0.101	0.02	0.991	0.70	7.12	0.982
^{137}Cs	303	41.81	0.015	0.116	0.995	0.61	1.47	0.983
	318	44.37	0.015	0.116	0.996	0.63	1.46	0.979
	333	46.06	0.016	0.112	0.989	0.62	1.56	0.986
$^{152+154}$Eu	303	39.00	0.012	0.143	0.993	0.63	1.09	0.975
	318	40.21	0.012	0.139	0.996	0.62	1.18	0.982
	333	42.11	0.014	0.129	0.996	0.62	1.30	0.981

Table 6 Comparison of the monolayer capacity of ^{137}Cs, $^{152+154}$Eu, and ^{131}Ba sorbed onto various sorbents

Sorbents	Shaking time [min]	Q_{max} [mg g^{-1}]			Ref. no
		^{131}Ba	^{137}Cs	$^{152+154}$Eu	
IPT	240	64.47	41.81	39.0	Current work
Dolomite powder	120	3.96	NR	NR	[59]
MXene	120	9.3	NR	NR	[60]
SP(M) (miswak powder)	60	34.97	NR	NR	[15]
SnSiMo	15	NR	16.14	NR	[65]
SnV	120	NR	26.68	NR	[61]
PAM/TiWSi	120	NR	30.7	26.6	[62]
Activated carbon	90	NR	NR	18.41	[63]
B:D composite	1440	NR	NR	26.87	[64]

structure and unfavorable Freundlich adsorption processes [52]. The results of ^{137}Cs, $^{152+154}$Eu, and ^{131}Ba sorbed onto IPT sorbent by Langmuir and Freundlich isotherms were shown in Fig. 8. As well as the constants of both isotherm models were calculated from the slope and intercept, and the data were tabulated in Table 5. The R^2 values obtained from Freundlich for ^{131}Ba, ^{137}Cs, and $^{152+154}$Eu were lower than the Langmuir isotherm values. Based on R^2 data, the linear forms of the Freundlich model were less applicable than the Langmuir model.

Literature review of monolayer sorption capacity of different sorbents

The monolayer capacity (Q_{max}) of IPT sorbent for the sorption of ^{137}Cs, $^{152+154}$Eu, and ^{131}Ba was compared with other sorbents reported in the literature. As characterized in Table 6, the monolayer capacity of IPT is a good value compared with the previously reported values which recommended that this is a promising material to decontaminate ^{137}Cs, $^{152+154}$Eu, and ^{131}Ba from aqueous media [15, 35, 59–66].

Effect of temperature studies

The linear form between ln K_d of ^{137}Cs, $^{152+154}$Eu, and ^{131}Ba onto IPT sorbent and 1000/T was exposed in Fig. 9 according to Van't Hoff relation [24]:

$$\ln K_d = \frac{\Delta S^o}{R} - \frac{\Delta H^o}{RT}$$

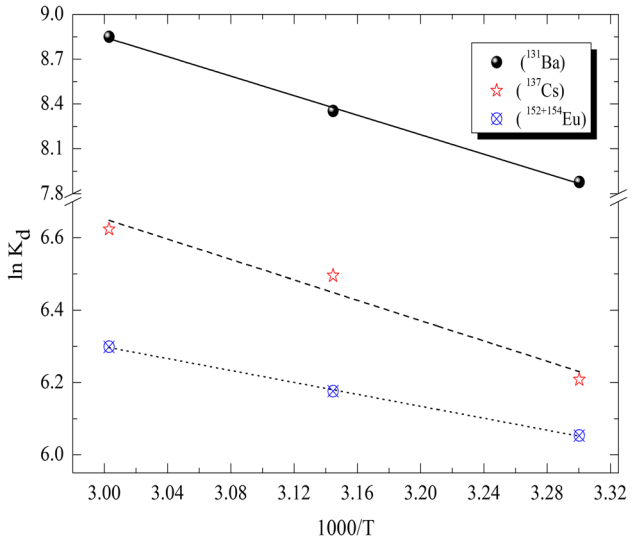

Fig. 9 A plot of ln K_d against 1000/T for sorption of ^{137}Cs, $^{152+154}$Eu, and ^{131}Ba onto IPT sorbent [C_i = 50 mg L^{-1}, V/m = 0.1 L g^{-1}, pH = 6 for ^{131}Ba and ^{137}Cs and pH = 4 for.$^{152+154}$Eu]

Table 7 Thermodynamic parameters for the sorption of ^{137}Cs, $^{152+154}$Eu, and ^{131}Ba onto IPT sorbent

Radionuclides	Temp [K]	ΔH° [kJ mol^{-1}]	ΔS° [J mol^{-1} K^{-1}]	ΔG° [kJ mol^{-1}]
^{131}Ba	303	27.2	155.0	− 19.8
	318			− 22.1
	333			− 24.5
^{137}Cs	303	11.7	90.4	− 15.7
	318			− 17.0
	333			− 18.4
$^{152+154}$Eu	303	6.9	72.9	− 15.2
	318			− 16.3
	333			− 17.4

where R, ΔH°, T, and ΔS° are the gas constant, the enthalpy change of adsorption, the absolute temperature, and the entropy change of adsorption, respectively. As exposed in Fig. 9, ln K_d of ^{137}Cs, $^{152+154}$Eu, and ^{131}Ba increased with rising reaction temperature from 303 to 333 K. This enhancement is due to the acceleration of previously slow adsorption steps and the formation of new active sites on adsorbent surfaces [52]. From both slopes and intercepts of the straight lines, ΔH° and ΔS° were obtained and tabulated in Table 7. The positive values of ΔH° and ΔS° reflect the endothermic nature of the adsorption process and the increased randomness of the solid solution interface during the adsorption of ^{137}Cs, $^{152+154}$Eu, and ^{131}Ba onto IPT sorbent, respectively [24, 52, 67]. The free energy change of specific adsorption (ΔG°) was obtained using the relation:

$$\Delta G^o = \Delta H^o - T\Delta S^o \quad (13)$$

The negative values of ΔG° reflect the adsorption process is spontaneous and reflects the preferable adsorption of ^{137}Cs, $^{152+154}$Eu, and ^{131}Ba onto IPT sorbent compared with the H^+ ion [67].

Conclusion

The co-precipitation method was used to prepare IPT sorbent. IPT sorbent was characterized and employed for batch sorption of ^{137}Cs, $^{152+154}$Eu, and ^{131}Ba from an aqueous solution. The sorption data of ^{137}Cs, $^{152+154}$Eu, and ^{131}Ba reveal that IPT has an equilibrium time for ^{137}Cs and $^{152+154}$Eu (1 h) and ^{131}Ba (5 h). The optimal pH = 4 for $^{152+154}$Eu and pH = 6 for ^{131}Ba and ^{137}Cs. The pseudo-2nd-order kinetic described the kinetic data well, reflecting the presence of chemisorption. Isotherm models are more applicable for the Langmuir model with high monolayer

capacity for studied radionuclides. Thermodynamic functions show the adsorption of ^{137}Cs, $^{152+154}$Eu, and ^{131}Ba onto IPT sorbent was endothermic and spontaneous. Finally, IPT sorbent could be considered a promising sorbent possessing high sorptive abilities for the studied radionuclides.

Acknowledgements This work has been supported by the Egyptian Atomic Energy Authority.

Author contributions Muhammad S. Mansy: experimental work, reviewing, and editing. Marwa A. Eid: experimental work and editing. Mohamed M.E. Breky: experimental work and editing. Mohamed R. Abass: Data curation, preparing sorbent, writing—original draft review and editing.

Funding Not applicable.

Availability of data and materials Yes.

Declarations

Conflict of interest The authors whose names are listed immediately below certify that they have NO affiliations with or involvement in any organization or entity with any financial interest (such as honoraria; educational grants; participation in speakers' bureaus; membership, employment, consultancies, stock ownership, or other equity interest; and expert testimony or patent-licensing arrangements), or non-financial interest (such as personal or professional relationships, affiliations, knowledge or beliefs) in the subject matter or materials discussed in this manuscript.

Consent to publish Yes.

Consent to participate Yes.

Ethical approval Yes.

References

1. Zhang H, Zhu M, Du X et al (2021) Removal of cesium from radioactive waste liquids using geomaterials. Appl Sci 11:8407
2. Mezga LJ (1990) Standardization of radioactive waste categories. Oak Ridge Gaseous Diffusion Plant, TN (USA)
3. Hamed MM, Holiel M, Ismail ZH (2016) Removal of ^{134}Cs and $^{152+154}$Eu from liquid radioactive waste using Dowex HCR-S/S. Radiochim Acta 104:399–413
4. Roy K, Pal DK, Basu S, Nayak D, Lahiri S (2002) Synthesis of a new ion exchanger, zirconiums vanadate, and its application to the separation of barium and cesium radionuclides at tracer levels. Appl Radiat Isot Isot 57:471–475
5. Hassan HS, Kenawy SH, El-Bassyouni GT et al (2020) Sorption behavior of cesium and europium radionuclides onto nano-sized calcium silicate. Part Sci Technol 38:105–112
6. Majidnia Z, Idris A, Majid M et al (2015) Efficiency of barium removal from radioactive wastewater using the combination of maghemite and titania nanoparticles in PVA and alginate beads. Appl Radiat Isot 105:105–113
7. Abass MR, El-Masry EH, El-Kenany WM (2022) Gamma irradiation-induced preparation of polyacrylonitrile acrylamide nano-silica for removal of some hazardous metals. J Inorg Organomet Polym Mater 32:536–546
8. Eid MA, Abass MR, El-Kenany WM (2022) Fabrication and application of nanosized stannic oxide for sorption of some hazardous metal ions from aqueous solutions. Radiochim Acta 110:1003–1015
9. Hodkin DJ, Stewart DI, Graham JT, Burke IT (2016) Coprecipitation of 14C and Sr with carbonate precipitates: the importance of reaction kinetics and recrystallization pathways. Sci Total Environ 562:335–343
10. Jia F, Yin Y, Wang J (2018) Removal of cobalt ions from simulated radioactive wastewater by vacuum membrane distillation. Prog Nucl Energy 103:20–27
11. Chiera NM, Bolisetty S, Eichler R et al (2021) Removal of radioactive cesium from contaminated water by whey protein amyloids-carbon hybrid filters. RSC Adv 11:32454–32458
12. Hurtado-Bermúdez S, Villa-Alfageme M, Mas JL, Alba MD (2018) Comparison of solvent extraction and extraction chromatography resin techniques for uranium isotopic characterization in high-level radioactive waste and barrier materials. Appl Radiat Isot 137:177–183
13. Naeimi S, Faghihian H (2017) Performance of novel adsorbent prepared by magnetic metal-organic framework (MOF) modified by potassium nickel hexacyanoferrate for removal of Cs^+ from aqueous solution. Sep Purif Technol 175:255–265
14. Zhang L, Wei J, Zhao X et al (2015) Adsorption characteristics of strontium on synthesized antimony silicate. Chem Eng J 277:378–387
15. Hassan SSM, Kamel AH, Youssef MA et al (2020) Removal of barium and strontium from wastewater and radioactive wastes using a green bioadsorbent, Salvadora persica (Miswak). Desalin Water Treat 192:306–314
16. Xie H, Zhang S, Zhong L et al (2021) Effect of the occurrence state of magnesium in talc on the adsorption of Pb(II). J Alloys Compd 887:161288
17. Abass MR, El-Kenany WM, El-Masry EH (2022) High efficient removal of lead(II) and cadmium(II) ions from multi-component aqueous solutions using polyacrylic acid acrylonitrile talc nanocomposite. Environ Sci Pollut Res 29:72929–72945
18. Sani HA, Ahmad MB, Saleh TA (2016) Synthesis of zinc oxide/talc nanocomposite for enhanced lead adsorption from aqueous solutions. RSC Adv 6:108819–108827
19. Hagag MS, Esmaeel SM, Salem F et al (2022) Uranium sorption from waste solutions by Talc Phosphogypsum ferri-silicate synthetic new sorbent. Radiochim Acta 110:93–106
20. Basuki T, Nakashima S (2021) Cs adsorption and CsCl particle formation facilitated by amino talc-like clay in aqueous solutions at room temperature. ACS Omega 6:26026–26034
21. Sprynskyy M, Kowalkowski T, Tutu H et al (2011) Adsorption performance of talc for uranium removal from aqueous solution. Chem Eng J 171:1185–1193
22. Kalantari K, Ahmad MB, Masoumi HRF et al (2014) Rapid adsorption of heavy metals by Fe_3O_4/talc nanocomposite and optimization study using response surface methodology. Int J Mol Sci 15:12913–12927
23. Wenlei L, Shanlin Z, Shuang C et al (2014) Adsorptive characteristics of modified talcum powder in removing methylene blue from wastewater. Chem Speciat Bioavailab 26:167–175
24. Abass MR, Maree RM, Sami NM (2022) Adsorptive features of cesium and strontium ions on zirconium tin(IV) phosphate nanocomposite from aqueous solutions. Int J Environ Anal Chem 1–20
25. Abass MR, Ibrahim AB, Abou-Mesalam MM (2021) Retention and selectivity behavior of some lanthanides using bentonite dolomite as a natural material. Chem Pap 75:3751–3759
26. Hamed MM, Shahr El-Din AM, Abdel-Galil EA (2019) Nanocomposite of polyaniline functionalized Tafla: synthesis, characterization, and application as a novel sorbent for selective removal of Fe(III). J Radioanal Nucl Chem 322:663–676

27. Abass MR, Ibrahim AB, El-Masry EH, Abou-Mesalam MM (2021) Optical properties enhancement for polyacrylonitrile-ball clay nanocomposite by heavy metals saturation technique. J Radioanal Nucl Chem 329:849–855
28. Kasem AE, Abdel-Galil EA, Belacy N, Badawy NA (2021) Kinetics and adsorption equilibrium of some radionuclides on polyaniline/SiO_2 composite. Radiochim Acta 109:85–97
29. Gupta VK, Agarwal S, Tyagi I et al (2015) Synthesis, characterization and analytical application of cellulose acetate tin(IV) molybdate nanocomposite ion exchanger: binary separation of heavy metal ions and antimicrobial activity. Ionics 21:2069–2078
30. Hassan RS, Abass MR, Eid MA, Abdel-Galil EA (2021) Sorption of some radionuclides from liquid waste solutions using anionic clay hydrotalcite sorbent. Appl Radiat Isot 178:109985
31. Metwally SS, Hassan HS, Samy NM (2019) Impact of environmental conditions on the sorption behavior of ^{60}Co and $^{152+154}$Eu radionuclides onto polyaniline/zirconium aluminate composite. J Mol Liq 287:110941
32. Mahrous SS, Abdel-Galil EA, Mansy MS (2022) Investigation of modified orange peel in the removal of Cd^{2+}, Co^{2+} and Zn^{2+} from wastewater. J Radioanal Nucl Chem 331:985–997
33. Abou-Mesalam MM, Abass MR, Abdel-Wahab MA et al (2018) Polymeric composite materials based on silicate: II. sorption and distribution studies of some hazardous metals on irradiated doped polyacrylamide acrylic acid. Desalin Water Treat 109:176–187
34. Hassan RS, Eid MA, El-Sadek AA, Mansy MS (2019) Preparation, characterization and application of Mg/Fe Hydrotalcite as gamma sealed source for spectroscopic measurements. Appl Radiat Isot 151:74–80
35. Mansy MS, Hassan RS, Selim YT, Kenawy SH (2017) Evaluation of synthetic aluminum silicate modified by magnesia for the removal of ^{137}Cs, ^{60}Co and $^{152+154}$Eu from low-level radioactive waste. Appl Radiat Isot 130:198–205
36. Comodi P, Zanazzi PF (1993) Structural study of ellenbergerite. Part II: effects of high pressure. Eur J Miner 5:831–838
37. Taha KK, Suleiman TM, Musa MA (2011) Performance of Sudanese activated bentonite in bleaching cottonseed oil. J Bangladesh Chem Soc 24:191–201
38. Andrunik M, Bajda T (2019) Modification of bentonite with cationic and nonionic surfactants: structural and textural features. Materials 12:3772
39. Alabarse FG, Conceição RV, Balzaretti NM et al (2011) In-situ FTIR analyses of bentonite under high-pressure. Appl Clay Sci 51:202–208
40. Rao KTV, Souzanchi S, Yuan Z et al (2017) Simple and green route for preparation of tin phosphate catalysts by solid-state grinding for dehydration of glucose to 5-hydroxymethylfurfural (HMF). RSC Adv 7:48501–48511
41. Xu Y, Zhou F, Chen M et al (2020) Facile assembly of 2D α-zirconium phosphate supported silver nanoparticles: superior and recyclable catalysis. New J Chem 44:9793–9801
42. Abdel-Galil EA, Eid MA, Hassan RS (2020) Preparation of nano-sized stannic silicomolybdate for chromatographic separation of Y(III) from Zr(IV). Part Sci Technol 38:113–120
43. Abdel-Galil EA, Ibrahim AB, El-Kenany WM (2021) Facile fabrication of a novel silico vanadate ion exchanger: evaluation of its sorption behavior towards europium and terbium ions. Desalin Water Treat 226:303–318
44. Ibrahim AB, Abass MR, EL-Masry EH, Abou-Mesalam MM, (2021) Gamma radiation-induced polymerization of polyacrylic acid-dolomite composite and applications for removal of cesium, cobalt, and zirconium from aqueous solutions. Appl Radiat Isot 178:109956
45. Abou-Mesalam MM, Abass MR, Abdel-Wahab MA et al (2016) Complex doping of d-block elements cobalt, nickel, and cadmium in magneso-silicate composite and its use in the treatment of aqueous waste. Desalin Water Treat 57:25757–25764
46. Metwally SS, Hassan RS, El-Masry EH, Borai EH (2018) Gamma-induced radiation polymerization of kaolin composite for sorption of lanthanum, europium and uranium ions from lowgrade monazite leachate. J Radioanal Nucl Chem 315:39–49
47. Moloukhia H (2010) Use of animal charcoal prepared from the bivalve chaelatura (chaelatura) companyoi in treatment of waste solution containing cesium and strontium ions. J Radiat Res Appl Sci 3:343–356
48. Abou-Mesalam MM, Abass MR, Ibrahim AB, Zakaria ES (2020) Polymeric composite materials based on silicate. III-Capacity and sorption behavior of some hazardous metals on irradiated doped polyacrylamide acrylonitrile. Desalin Water Treat 193:402–413
49. El-Naggar IM, Sheneshen ES, Abdel-Galil EA (2016) Diffusion mechanism of Co^{2+}, Cu^{2+}, Cd^{2+}, Cs^{+}, and Pb^{2+} ions in the particles of polyaniline silicotitanate. Part Sci Technol 34:373–379
50. Sheha RR, El-Zahhar AA (2008) Synthesis of some ferromagnetic composite resins and their metal removal characteristics in aqueous solutions. J Hazard Mater 150:795–803
51. Borai EH, Attallah MF, Elgazzar AH, El-Tabl AS (2019) Isotherm and kinetic sorption of some lanthanides and iron from aqueous solution by aluminum silicotitante exchanger. Part Sci Technol 37:414–426
52. Abdel-Galil EA, Ibrahim AB, Abou-Mesalam MM (2016) Sorption behavior of some lanthanides on polyacrylamide stannic molybdophosphate as organic-inorganic composite. Int J Ind Chem 7:231–240
53. El-Deen SEAS, Moussa SI, Mekawy ZA et al (2017) Evaluation of CNTs/MnO_2 composite for adsorption of ^{60}Co(II), ^{65}Zn(II) and Cd(II) ions from aqueous solutions. Radiochim Acta 105:43–55
54. Ahmed IM, Aglan RF, Hamed MM (2017) Removal of Arsenazo-III and Thorin from radioactive waste solutions by adsorption onto low-cost adsorbent. J Radioanal Nucl Chem 314:2253–2262
55. Karaca S, Gürses A, Açışlı Ö et al (2013) Modeling of adsorption isotherms and kinetics of Remazol Red RB adsorption from aqueous solution by modified clay. Desalin Water Treat 51:2726–2739
56. Dakroury GA, El-Shazly EAA, Hassan HS (2021) Preparation and characterization of ZnO/Chitosan nanocomposite for Cs(I) and Sr(II) sorption from aqueous solutions. J Radioanal Nucl Chem 330:159–174
57. Manjuladevi M, Anitha R, Manonmani S (2018) Kinetic study on adsorption of Cr(VI), Ni(II), Cd(II) and Pb(II) ions from aqueous solutions using activated carbon prepared from Cucumis melo peel. Appl Water Sci 8:1–8
58. Abass MR, El-Masry EH, Ibrahim AB (2021) Preparation, characterization, and applications of polyacrylonitrile/ball clay nanocomposite synthesized by gamma radiation. Environ Geochem Health 43:3169–3188
59. Ghaemi A, Torab-Mostaedi M, Ghannadi-Maragheh M (2011) Characterizations of strontium(II) and barium(II) adsorption from aqueous solutions using dolomite powder. J Hazard Mater 190:916–921
60. Fard AK, Mckay G, Chamoun R et al (2017) Barium removal from synthetic natural and produced water using MXene as two dimensional (2-D) nanosheet adsorbent. Chem Eng J 317:331–342
61. Abass MR, Breky MME, Maree RM (2022) Removal of ^{137}Cs and ^{90}Sr from simulated low-level radioactive waste using tin(IV) vanadate sorbent and its potential hazardous parameters. Appl Radiat Isot 189:110417
62. Mahrous SS, Mansy MS, Abdel Galil EA (2022) Decontamination of ^{137}Cs, ^{95}Zr, ^{154}Eu and ^{144}Ce from aqueous solutions using polyacrylamide titanium tungstosilicate. J Radioanal Nucl Chem 1–14
63. Omar HA, Moloukhia H (2008) Use of activated carbon in removal of some radioisotopes from their waste solutions. J Hazard Mater 157:242–246

64. Abass MR, Ibrahim AB, Abou-Mesalam MM (2022) Sorption and selectivity behavior of some rare earth elements on bentonite-dolomite composites as natural materials. Radiochemistry 64:349–359
65. Abdel-Galil EA, Hassan RS, Eid MA (2019) Assessment of nano-sized stannic silicomolybdate for the removal of ^{137}Cs, ^{90}Sr, and ^{141}Ce radionuclides from radioactive waste solutions. Appl Radiat Isot 148:91–101
66. Mahrous SS, Abass MR, Mansy MS (2022) Bentonite phosphate modified with nickel: preparation, characterization, and application in the removal of ^{137}Cs and $^{152+154}$Eu. Appl Radiat Isot 190:110445
67. El-Naggar IM, Mowafy EA, Abdel-Galil EA, El-Shahat MF (2010) Synthesis, characterization and ion-exchange properties of a novel 'organic–inorganic' hybrid cation-exchanger: polyacrylamide Sn(IV) molybdophosphate. Glob J Phys Chem 1:91–106